POLITECNICO DI TORINO
Repository ISTITUZIONALE

Plasmonically-enhanced all-optical integrated phase-change memory

Original
Plasmonically-enhanced all-optical integrated phase-change memory / Gemo, E., Carrillo, S.G.-C., Degalarreta, C.R., Baldycheva, A., Hayat, H., Youngblood, N., Bhaskaran, H., Pernice, W.H.P., Wright, C.D.. - In: OPTICS EXPRESS. - ISSN 1094-4087. - ELETTRONICO. - 27:17(2019), pp. 24724-24738. [10.1364/OE.27.024724]

Availability:
This version is available at: 11583/2989980 since: 2024-06-28T19:54:57Z

Publisher:
Optica Publ.

Published
DOI:10.1364/OE.27.024724

Terms of use:

This article is made available under terms and conditions as specified in the corresponding bibliographic description in the repository

Publisher copyright

(Article begins on next page)

25 November 2026

Research Article | Vol. 27, No. 17 | 19 Aug 2019 | OPTICS EXPRESS 24724
Optics EXPRESS

Plasmonically-enhanced all-optical integrated phase-change memory

EMANUELE GEMO,[1] SANTIAGO GARCIA-CUEVAS CARRILLO,[1] CARLOTA RUIZ DEGALARRETA,[1] ANNA BALDYCHEVA,[1] HASAN HAYAT,[1,2] NATHAN YOUNGBLOOD,[3] HARISH BHASKARAN,[3] WOLFRAM H. P. PERNICE,[4] AND C. DAVID WRIGHT[1,*]

[1]*Department of Engineering, University of Exeter, UK*
[2]*College of Engineering, Swansea University, UK*
[3]*Department of Materials, University of Oxford, UK*
[4]*Institute of Physics, University of Münster, Germany*
**david.wright@exeter.ac.uk*

Abstract: Integrated phase-change photonic memory devices offer a novel route to non-volatile storage and computing that can be carried out entirely in the optical domain, obviating the necessity for time and energy consuming opto-electrical conversions. Such memory devices generally consist of integrated waveguide structures onto which are fabricated small phase-change memory cells. Switching these cells between their amorphous and crystalline states modifies significantly the optical transmission through the waveguide, so providing memory, and computing, functionality. To carry out such switching, optical pulses are sent down the waveguide, coupling to the phase-change cell, heating it up, and so switching it between states. While great strides have been made in the development of integrated phase-change photonic devices in recent years, there is always a pressing need for faster switching times, lower energy consumption and a smaller device footprint. In this work, therefore, we propose the use of plasmonic enhancement of the light-matter interaction between the propagating waveguide mode and the phase-change cell as a means to faster, smaller and more energy-efficient devices. In particular, we propose a form of plasmonic dimer nanoantenna of significantly sub-micron size that, in simulations, offers significant improvements in switching speeds and energies. Write/erase speeds in the range 2 to 20 ns and write/erase energies in the range 2 to 15 pJ were predicted, representing improvements of one to two orders of magnitude when compared to conventional device architectures.

Published by The Optical Society under the terms of the Creative Commons Attribution 4.0 License. Further distribution of this work must maintain attribution to the author(s) and the published article's title, journal citation, and DOI.

1. Introduction

Optical signaling has dominated long-distance communications for decades. More recently, chip-to-chip and even on-chip optical signaling have gained traction, in particular due to the rising influence of silicon photonics [1–3]. Indeed, moving to all-optical implementations for key on-chip data operations can potentially save energy and increase speeds, by making electrical-optical conversions redundant and accessing the high-bandwidths and low transmission losses inherent to the optical domain. One such key data operation is the provision of binary and/or multilevel memory. While promising approaches to the realization of integrated photonic memories have been developed over the years (see e.g [4–6].), these led to devices that were essentially inherently volatile, often requiring a steady energy-consuming optical bias to preserve the stored state. All-optical non-volatile storage using an integrated photonic platform has however recently been reported, by using chalcogenide phase-change materials (PCMs) as the active, but non-volatile, memory element [7–11].

#369553 https://doi.org/10.1364/OE.27.024724
Journal © 2019 Received 7 Jun 2019; revised 24 Jul 2019; accepted 24 Jul 2019; published 15 Aug 2019

Optics EXPRESS

Indeed, by incorporating PCM cells into chip-scale photonic devices, all-optical arithmetic processing, neuromorphic and in-memory computing are also possible [12–14].

In such memory and processing applications using integrated phase-change photonic devices, the basic mode of operation involves switching, using light guided down an integrated waveguide, the PCM cell between its crystalline and amorphous states (or to intermediate states between the two). Such switching results in a non-volatile and reversible modification of the waveguide's optical transmission, thus forming the basis of the readout process - see Fig. 1(a). Accomplishing such switching in the shortest possible timescales and with the smallest amount of energy is a major design goal. In very recent work, it has been shown that switching times and energies can be lowered considerably by a number of approaches, such as by judicious tailoring of the shape of the optical write/erase pulses [10] or the use of photonic crystal cavity waveguides [15]. Here we explore, via simulation, another attractive alternative, namely the use of plasmonic enhancement of the optical field that interacts with the PCM cell.

The combination of plasmonics with photonic integrated circuits (PICs) is a growing field, with applications aimed at reducing the size (and improving the performance) of PICs [16–19], developing novel types of sensors [20–22] and realizing quantum computing [23,24]. Some encouraging preliminary studies of the interaction of PCMs with both localized and surface plasmonic resonances have also been reported [25,26].

Here, we introduce plasmonics into the integrated phase-change photonic memory by placing a plasmonic dimer nanoantenna on top of the integrated waveguide and depositing phase-change materials in the space between the two halves of the nanoantenna, as shown in Fig. 1(b). As we show in §3, the plasmonic nanoantenna greatly enhances the interaction between the electromagnetic field of the waveguide propagating mode and the phase-change cell. This, coupled with a substantial reduction in the volume of phase-change material that undergoes switching (as compared to the conventional approach of Fig. 1(a)), leads to quite dramatic improvements in both switching speed and energy consumption.

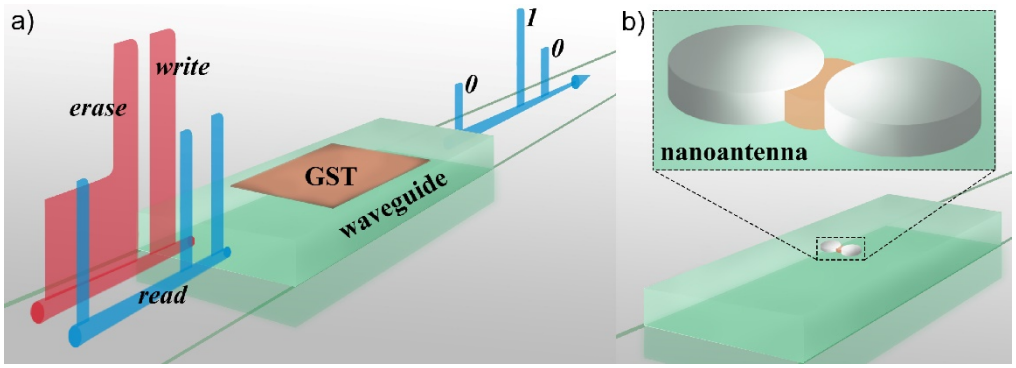

Fig. 1. Integrated phase-change photonic memory, configuration and operation schematics. The memory level 1 or 0 is encoded in the phase-state (amorphous or crystalline) of the phase-change cell (here made from $Ge_2Sb_2Te_5$, or GST for short). *Read* and *write/erase* are performed via delivery of optical laser pulses through an integrated waveguide; the optical absorption provided by GST provides both signal modulation for *read* operations and the heat source for *write/erase* operations. (a) Conventional configuration, consisting of (typically) a micrometer-scale phase-change cell deposited on top of the waveguide. (b) The proposed plasmonically-enhanced configuration, consisting of a metallic dimer nanoantenna, with the phase-change material deposited within the nanoantenna gap.

2. Methods

As shown in Fig. 1(b), our proposed plasmonic device consists of a dimer nanoantenna, comprising two metallic nanodiscs on top of a rib waveguide (here a silicon nitride waveguide, but the concept is also transferable to silicon waveguides), with a phase-change

Optics EXPRESS

material (here the well-known composition $Ge_2Sb_2Te_5$, or GST for short) deposited into the antenna gap. A range of suitable plasmonic metals could be used for antenna fabrication: here, by way of proof-of-concept, we choose silver, since it is known to have excellent plasmonic properties at near-infrared wavelengths [27]. However, we do note that the archetypal plasmonic metals of Au and Ag tend to diffuse into chalcogenides, resulting in adverse changes in the latter's optical and electrical properties [28]. Such diffusion can be eliminated by the insertion of appropriate barrier layers [28,29] (with such layers not adversely affecting overall optical performance).

The most significant factors influencing the plasmonic behavior of the device of the type shown in Fig. 1(b) will be the radius, r, and thickness, t, of the nanodiscs, the size, g, of the gap between them and of course the constituent properties of the materials used. To understand the importance of these factors we simulated their effect on the plasmonically-induced local field enhancement and the waveguide transmitted optical power (the latter corresponding to the readout signal when the device is used as a memory, see Fig. 1(a)), as well as on the device's reflection, absorption and scattering properties. Simulations were carried out using finite element modeling (FEM) in the software package COMSOL.

In detail, the device (as used in previous published works, see e.g [9].) consists of a Si_3N_4 rib waveguide (1300 nm x 170 nm) fabricated on top of a SiO_2 substrate. A silver plasmonic dimer nanoantenna (with varying nanodisc radius, thickness and gap spacing) is deposited in the center of the waveguide, with the gap between the antenna's nanodiscs filled with a thin layer of GST. The propagating optical mode in the waveguide is specified as TE and of wavelength 1550 nm. The optical model is solved in COMSOL, using the RF (radio frequency) module. We apply a 2nd order boundary scattering condition [30] at the outer surfaces to avoid any unphysical reflections, and we use a perfect electric conductor boundary condition along the model cut plane to mirror the calculated solution (so reducing computation time by exploiting the natural symmetry of the device structure). Source and listener ports are placed at the extremal surfaces, normal to the waveguide.

Heat diffusion calculations are carried out using the COMSOL HT (heat transfer) module. The bottom surface of the substrate and both waveguide section surfaces normal to the waveguide axis (and at the extremities of the simulated volume) were fixed at room temperature, while all other surfaces were considered as thermally insulating. Since, it is well known that thermal boundary resistance (TBR) effects are significant in chalcogenide phase-change devices, we include a thermal boundary resistance condition for the GST domain ($TBR_{GST} = 3 \times 10^{-8}$ m^2K/W [31,32]), the Si_3N_4-Ag interface ($TBR = 5 \times 10^{-9}$ m^2K/W [33]), in addition to between the Si_3N_4 and SiO_2 substrate layer ($TBR = 1 \times 10^{-9}$ m^2K/W [34]). The volumetric source of heat, Q_V, arises from the optical losses caused by the GST cell and the nanodiscs of the nanoantenna itself.

For simulation of the phase-change process, i.e., writing and erasing (amorphizing and re-crystallizing) the GST cell, we use a method based on the well-known nucleation and growth crystallization model [35]. The phase-change model runs in MATLAB using purpose-written code, and is linked, at each relevant time step, to the optical and thermal COMSOL simulations described above. The various material parameters used in the simulations are given in Table 1.

Table 1. Material parameters list for the plasmonic integrated phase-change photonic device simulation

	Refractive index at 1550 nm	Specific Heat [J/K]	Thermal Conductivity [W/mK]	Density [Kg/m^3]
GST_{cry}	6.11* + 0.83i* [36]	210 [37]	0.58 [37]	6150 [38]
GST_{am}	3.94* + 0.045i* [36]		0.2 [37]	5780 [38,39]

Optics EXPRESS

Si_3N_4	1.98* [40]	774* [41]	18.4* [41]	2750 [42]
SiO_2	1.44 [43]	697* [41]	1.37* [41]	2270 [44]
Si	3.48 [45]	700 [44]	157 [44]	2330 [44]
Ag	0.145 + 11.445i [46]	235 [47]	145 [48]	10820 [49]

* Temperature dependent parameters; the stated value refers to room temperature.

3. Device operation and optimization

The basic operating concept of the device shown in Fig. 1(b) relies on the nanoantenna's capability to sustain a localized plasmonic resonance via coupling with the optical mode propagating in the waveguide. This plasmonic resonance results in a very substantial enhancement of the electric field in the gap region, as compared to the case of the conventional integrated phase-change photonic cell of the type shown in Fig. 1(a). Such enhancement leads, in turn, to magnification of the interaction between the phase-change cell and propagating light, ultimately improving energy consumption and switching speed in memory applications.

An example of the form of the plasmonic local field enhancement is shown in Fig. 2. Here we show various cross-sections of the nanoantenna and plot the log of the norm of the E-field in its vicinity, for the case of a nanodisc radius of 75 nm, a thickness of 30 nm and a gap spacing of 40 nm, with the gap filled with a 30 nm thick layer of GST. It is clear from Fig. 2 that the E-field is strongly localized in the antenna gap, for GST in both crystalline and amorphous phases (it is also considerably enhanced in strength *cf.* conventional case).

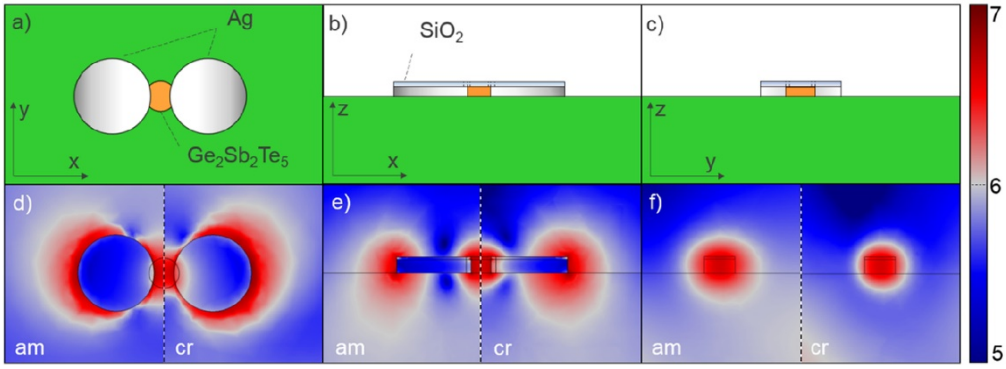

Fig. 2. Plasmonically-enhanced all-photonic phase-change memory device: concept and electric field distribution. (a –c) Cross sections of the photonic memory across xy, yz and yz planes respectively; each plane cuts the plasmonic nanoantenna at its center. (d –f) Log_{10} of electric field norm (colorbar on the right) due to TE propagating waveguide mode of 1 mW power, along the planes corresponding to Figs. 2(a), 2(b) and 2(c) respectively (figures depict the electric field at room temperature for amorphous (left) and crystalline (right) states of the GST cell).

To explore the field enhancement induced by the plasmonic antenna in more detail, we now examine its behavior in the absence of any phase-change cell. For this we calculate a quantitative enhancement factor, *EF* [20], as $EF = |E_{LOC}|^2 \div |E_0|^2$, with E_{LOC} being the electric field norm evaluated within the nanogap, and E_0 the input electric field norm. Results are shown in Fig. 3(a), where, for this analysis, we fix the nanoantenna thickness and gap spacing to 10 nm but allow the nanodisc radius to vary in size up to 300 nm maximum. We observe how the *EF* displays distinct peaks, here for radii of 100 nm and 210 nm and corresponding to dipolar and quadrupolar plasmonic resonances (as can be seen in Figs. 3(b) and 3(c)). Also in Fig. 3(a), we show how the transmission, absorption and reflection in the waveguide vary as a function of the nanoantenna radius. The transmission, *T*, through the waveguide essentially follows the *EF* radius dependency, with dips in transmission

Optics EXPRESS

approximately coincident with the peaks in *EF*, though shifted to larger radii. The mismatch between *EF* and *T* peak positions arises from interference between the plasmonic resonant mode and propagating wave: at the position of peak *EF* the resonant mode and propagating mode are in phase, whereas at the minima in *T* these two modes are dephased by π/2. The scattering, reflection and absorption behavior, as might be expected, show peaks at approximately the same radii values as the transmission minima, with scattering here being the dominant optical loss contribution.

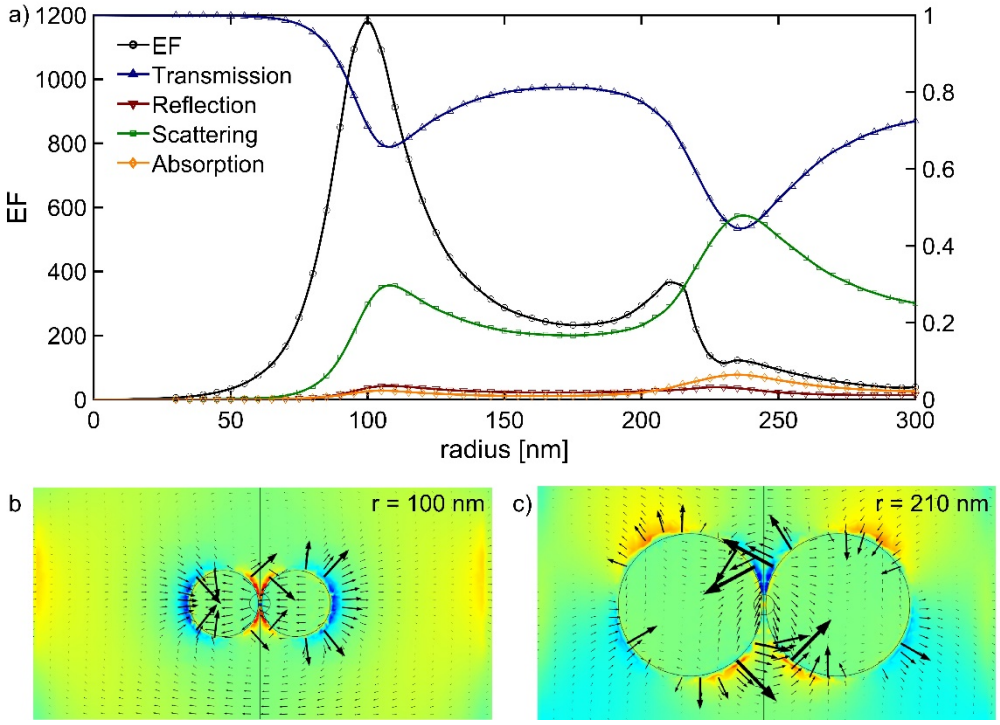

Fig. 3. Integrated nanoantenna optical properties (note no GST is present here, the gap between the antennas is 'filled' with air). (a) Enhancement factor *EF* (left axis), transmission *T*, reflection *R*, absorption *A* and scattering *S* (right axis) for a nanoantenna-only configuration, with disc thickness and gap size of 10 nm. A peak *EF* value of 1182 is observed for a disc radius value of 100 nm, while the transmission sees a local minimum ($T = 0.71$) at 110 nm. (b–c) Electric field magnitude, taken at the resonator cut plane passing through its center, and showing dipolar (b) and quadrupolar (c) plasmonic resonances at positions of the first and second peaks in *EF*. Color scale represents the strength of the field in the out-of-plane direction (red and blue have opposite signs), whereas the arrows depict the magnitude and direction of the field in-the-plane.

Optics EXPRESS

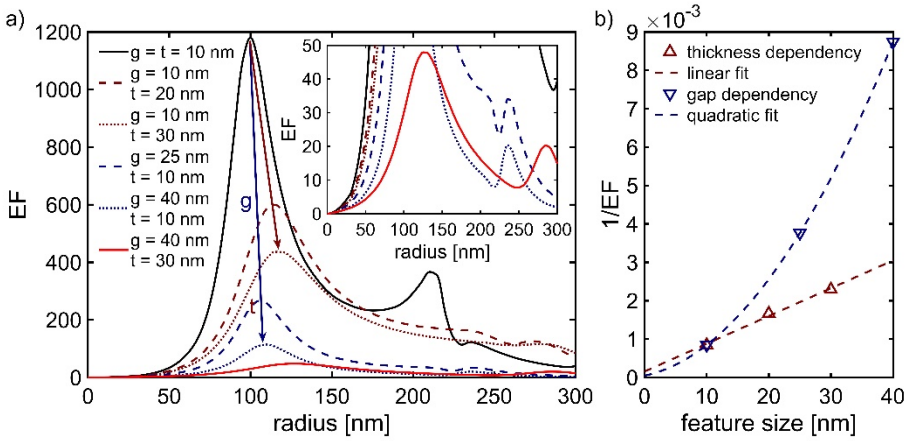

Fig. 4. *EF* configuration dependency analysis. (a) *EF* for different gap *g* and thickness *t* configurations of the nanoantenna (arrows are a guide to the eye towards the effect of each parameter increase). Inset shows a magnified version of the *g* = 40 nm, *t* = 30 nm configuration, which is considered in more detail in the text. (b) Dependency of $1/EF$ on gap size *g* (blue line) and disc thickness *t* (brown line).

Having explored the role of the nanoantenna radius on the properties of the plasmonically-enhanced waveguide, we now turn our attention to understanding the effects of other aspects of nanoantenna geometry, specifically the dependence of *EF* on the antenna's thickness and gap width. Exemplar results are shown in Fig. 4(a), where it is clear that increasing both the thickness and gap width of the antenna causes a decrease in *EF* (and a shift of peaks to slightly larger antenna radius), with the effect of the latter being more pronounced. Indeed, analyzing the reciprocal of *EF* versus the thickness/gap width reveals an approximate linear dependency with thickness but a quadratic dependency with the gap width; see Fig. 4(b). Since, from these results, it is clear that the plasmonic resonance is strongest for small antenna gap widths and thicknesses, we now examine the case for a nanoantenna with both thickness and gap width equal to 10 nm, but with the gap region now filled with the phase-change material GST (rather than just air). We also examine the case for more readily fabricated device sizes, specifically a gap width of 40 nm and film thicknesses of 30 nm.

The insertion of GST into the nanoantenna gap region will result in a dramatic change in the local refractive index, which in turn is expected to lead to a dramatic change in the nanoantenna resonance properties. Moreover, since the refractive index of GST (and other phase-change chalcogenides) differs very considerably between its crystalline and amorphous phase, the resonant properties of the nanoantenna should also be very different when the GST is its different phases. This is indeed the case, as we show in Fig. 5. For example, for *g* and *t* both equal to 10 nm, when the GST in its crystalline phase the dipolar plasmonic resonance occurs for an antenna radius of 55 nm (with two quadrupolar resonances at 170 nm and 240 nm). With the GST in its amorphous phase, the dipolar resonance occurs for *r* = 65 nm

Optics EXPRESS

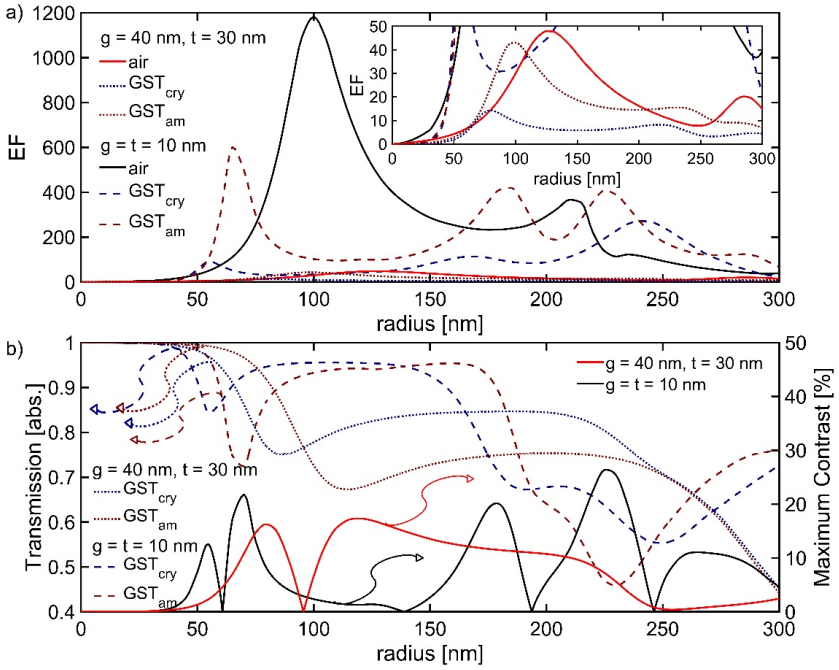

Fig. 5. Plasmonically-enhanced photonic phase-change cell optical properties. (a) *EF* for a nanoantenna of various gap widths and thicknesses and with the gap region filled with air and GST in both its crystalline and amorphous phases. Inset shows the g = 40 nm, t = 30 nm case in more detail. (b) Absolute transmission (left axis) for both crystalline and amorphous GST and (right axis) maximum readout contrast.

(quadrupolar resonances found at 185 nm and 225 nm). The resulting transmission through the waveguide with the GST in both phases, as well as the readout signal contrast (defined here as in [9], i.e. as $\frac{T_{am} - T_{cry}}{T_{am}}$, or, when $T_{cry} > T_{am}$, as $\frac{T_{cry} - T_{am}}{T_{cry}}$) is shown in Fig. 5(b). It is clear that a very strong signal contrast exists, even though here the active GST volume is several orders of magnitude smaller than in the case of a 'conventional' integrated phase-change photonic cell of Fig. 1(a). This is a direct result of the very substantial electric field enhancement in the active region resulting from the plasmonic resonance.

4. Memory performance

We have highlighted above how the proposed plasmonic device architecture provides an additional degree of freedom to magnify the interaction between the guided waveguide mode and a phase-change cell deposited on top of the waveguide. This in turn should lead to improvements in device performance when used as a non-volatile memory, specifically improvements in memory switching speed and energy consumption. We therefore now examine the memory performance of the plasmonic device during the *write* (i.e. amorphization) and *erase* (crystallization) processes. To *write* to the memory, a single relatively high-power optical pulse is sent down the waveguide that heats the phase-change cell to sufficiently high temperatures that it melts and, on cooling, freezes into the amorphous state. To *erase* the cell, the use of a single pulse is, as previously discussed [9], challenging in practice due to the substantial increase in absorption of the crystalline phase: if the phase transition occurs prior to the end of the single pulse, the continued high optical energy supply can melt the phase-change cell and lead to immediate re-amorphization. Thus, re-crystallization has generally been carried out in the literature with a train of optical pulses of

Optics EXPRESS

decreasing amplitude [8,9,12] though alternative approaches using suitably tailored 'double-step' pulses, where a first short and relatively high power pulse is followed immediately by a longer, low power, second pulse, are also possible (see [50]). Here we also use a double-step pulse approach, but with the second pulse having a gradually (linearly) decreasing power level, since this yields good control of the temperature in the phase-change cell itself.

In terms of the detailed structure of a device examined for memory performance, although above we have shown that small antenna gaps and small layer thicknesses lead to the largest field enhancement factors, the fabrication of actual devices with ultra-small gaps etc. is likely to be very challenging. We here therefore choose device sizes that are more practicable in terms of fabrication, namely a gap size, g, of 40 nm and layer thicknesses, t, of 30 nm. Should such relatively large device feature sizes lead to improved memory performance, then we can be quite confident that further shrinking of feature sizes (aided by advanced nanofabrication techniques), would result in even better performance. We also choose an antenna radius of 75 nm, corresponding to the appearance of the first (dipolar) plasmonic resonance (when the GST is in the crystalline phase), as shown in the inset of Fig. 5(a). The GST cell in our device simulations is assumed to fill the space between the antenna's two nanodiscs; more specifically here it comprises a would-be circle of radius r_{GST} = 30 nm, but omitting the regions that intersect with the nanodiscs. The whole structure is capped with 5 nm of SiO_2 for environmental protection. The waveguide itself, for consistency with previous work [9,10,12–14], is a Si_3N_4 rib waveguide of size 1300 nm × 170 nm on top of a SiO_2 substrate.

We begin by simulating the room-temperature transmission (T), reflection (R), scattering (S) and absorption (A) properties of the plasmonic memory device with the GST cell in its fully crystalline and fully amorphous states. These results mimic the *read* operation, performed by sending a low power optical pulse (which does not induce any significant heating) down the waveguide. The results are shown in Table 2, from which it is clear that the plasmonic cell yields a read signal contrast similar to, or even higher than, that seen in the conventional device configurations that incorporate much larger phase-change cells (see e.g [9].).

Table 2. Summary of plasmonic phase-change optical cell optical behavior at 1550 nm

	T	R	S	Total Absorption	GST Absorption	EF	% Signal contrast $[(T_{am}-T_{cry})/T_{am}]$
GST_{cry}	0.799	0.014	0.122	0.070	0.063	15.2	15.3%
GST_{am}	0.943	0.006	0.048	0.005	0.003	20.2	

Next, since plasmonic resonances can often be quite narrow (in wavelength/frequency terms), we check for the range of wavelengths over which the plasmonic device designed here might reliably operate. Specifically, we simulated the waveguide transmission and the signal contrast (for both crystalline and amorphous states of the GST cell) for a range of wavelengths spanning from the telecommunications O to L bands (specifically from 1300 nm to 1700 nm). Results are reported in Fig. 6, which confirms a resonant behavior centered, as designed, in the C band for crystalline GST, but also shows that the window of operating wavelengths is relatively large, with an eminently useable contrast of more than 10% obtained from around 1375 nm right out to 1650 nm.

Optics EXPRESS

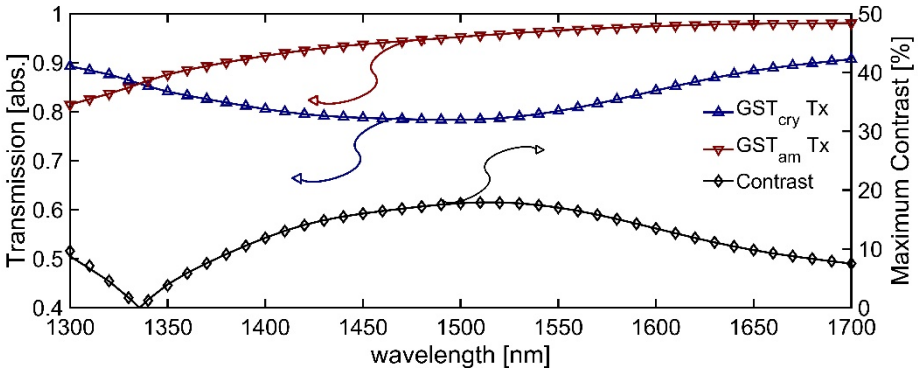

Fig. 6. Spectral response of the plasmonic phase-change cell across the 1300 nm – 1700 nm wavelength range. Left axis: absolute transmission (blue and brown lines, for crystalline and amorphous GST respectively). Right axis: maximum optical contrast. (Variation of refractive index as a function of wavelength taken from [51]).

We now turn our attention to the *write* process, i.e. the writing of an amorphous mark into a fully crystalline starting state. For this, we deliver a single 1.0 mW, 2 ns rectangular pulse along the waveguide. The pulse power has been optimized to induce a temperature peak lower than a notional damage threshold of 1500 K, and the resulting calculated peak intensity reaches values up to 6 MW/cm^2, very significantly lower than that reported to be necessary to induce GST ablation [52]. Results are plotted in Fig. 7. As shown in Fig. 7(a), on application of the write pulse the temperature in the GST increases rapidly, reaching, at the end of the pulse, an average temperature in excess of the melting temperature of GST (T_m = 893 K). Moreover, once the excitation pulse is removed (at 2 ns), the GST cell cools sufficiently rapidly for quenching into the amorphous phase (required cooling rates for successful amorphization of GST are in the region of tens of degrees per nanosecond, see e.g [53].). Indeed, successful amorphization is confirmed in Fig. 7(b) where we track the fraction, X, of crystallized material in the GST cell as a function of time. Initially the cell is fully crystalline (X = 1), but the amount of crystalline material in the cell (i.e. material that is neither in the amorphous phase nor melted) begins to reduce at 0.4 ns and settles at a low value of $X \approx 0.18$ directly after the end of the write pulse. The change of the fraction of crystallized material in the cell leads to a corresponding change in optical transmission through the waveguide, leading to an increase in signal contrast, as also shown in Fig. 7(b). The total energy delivered during the write process is here 2 pJ, and the total energy absorbed and scattered by the optical cell amounts to 340 fJ. These values are considerably smaller than those of the conventional (non-plasmonic) device, a point to which we return later. (Note that there is no physical impediment to achieving full amorphization (i.e. X = 0) during writing, but reaching such a state could be counterproductive from a memory perspective since it makes erasing significantly more difficult due to the low absorption of the amorphous phase).

Next, we consider the *erase* (i.e. re-crystallization) process. Here we deliver a 1.5 ns pulse of 1.5 mW, followed immediately by pulse with linearly decreasing power (of 1.2 mW to 0.5 mW) and a duration of 15 ns. The first part of this double-step pulse is designed to melt the cell, so as to provide a definitive starting state for re-crystallization. The second part of the pulse is designed to heat the majority of the cell up to a temperature conducive to fast crystallization, (typically between 600 and 700 K for GST, where the crystal growth rate is a maximum [54]). Thermal simulation results during erasure are shown in Fig. 7(c), where indeed it can be seen that the temperature in the in the GST cell is maintained above 600 K for the majority of the erase process. The total erase energy delivered is here 15 pJ, and the energy consumed by the optical cell is just 2.3 pJ. Note that after the application of the erase pulse (here ending at 16.5 ns), the cell returns quickly to room temperature (here after only

Optics EXPRESS

2.1 ns), indicating the rapid thermalization that is obtained in the plasmonic cell architecture (helped by the very small volumes of GST involved in the switching process in this case). Figure 7(d) shows the changes in crystal fraction and readout signal (optical contrast) during the above erase process, with a monotonic change in readout signal as the GST cell is re-crystallized, returning to the value of the initial starting (i.e., fully crystalline) state.

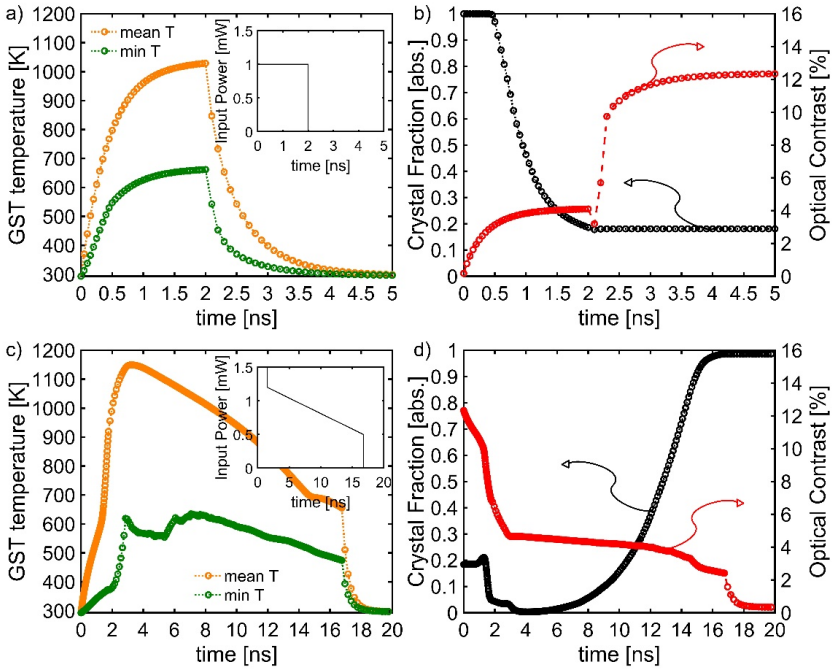

Fig. 7. Temperature, crystal fraction and readout contrast during *write* (amorphization) and *erase* (re-crystallization) operations. (a) Temperature evolution in the cell on application of a 1 mW, 2 ns *write* pulse (inset shows pulse details). (b) Crystal fraction and readout contrast during the *write* process. (c) Temperature evolution during application of a double-step erase pulse (1.5 mW for 1.5 ns, followed immediately by a 15 ns pulse with linearly decreasing power from 1.2 mW to 0.5 mW, as shown in inset). (d) Crystal fraction and readout contrast during the *erase* process.

It is clear from the above results that the plasmonic device has the potential for fast switching times and low switching energies. Indeed, comparing its predicted speed and energy performance to published experimental data for conventional integrated phase-change photonic memories (Table 3), quite significant improvements are evident. A potential drawback of the plasmonic approach is however a more difficult fabrication process, though with modern nanofabrication techniques such difficulties should not be insurmountable.

Table 3. Comparison of performance of various integrated phase-change photonic memory architectures

Configuration and GST cell size [μm]	Maximum contrast [%]	Shortest write/erase pulse [ns]	Thermal (1/e) dissipation time [ns]	Lowest pulse energy [pJ]	Figure-Of-Merit (Contrast/write energy) [10^{-3} dB/pJ]	Ref.
Ridge waveguide 0.25 × 1 × 0.01	0.67	Write:10 Erase: n/a	Write:10 Erase: n/a	n/s	Write: 0.52 Erase: n/a	[9]
Ridge waveguide 5 × 1 × 0.01	58	Write: 10 E: >1300	Write: 10 Erase: n/a	Write: 52 Erase: 3095	Write: 5.13 Erase: 0.46	[9]

Optics EXPRESS

Ridge waveguide 4 × 1.3 × 0.01	28	Write: 25 Erase:125	Write:200 Erase:500	Write: 68 Erase: 680	Write: 10.5 Erase: 2.09	[10]
Microring resonator 0.6 × 0.75 × 0.05	70	Write: 25 Erase: 2500	n/a	Write: 180 Erase: 1900	Write: 16.7 Erase: 1.58	[55]
Microring resonator 0.5 × 0.5 × 0.01 (× 5)	87	Write:50 Erase: 2500	n/a	Write: 220	Write: 40 Erase: n/a	[51]
PhC waveguide 0.91 × 1 × 0.01	96	Write: 100 Erase: >2500	n/a	Write: 150 Erase: 2160	Write: 10.6 Erase: n/a	[15]
Plasmonic nanoantenna 0.06 × 0.04 × 0.03	12.5	Write: 2 Erase: 16.5	Write: 0.6 Erase: 0.4	Write: 2 Erase: 15	Write: 289 Erase: 38.6	This work

In our discussions so far we have considered the operation of integrated phase-change photonic devices as binary memories. However, it has already been shown in the literature that the conventional rib waveguide architecture can readily yield multilevel memories; indeed, in [10] a 34-level memory was successfully demonstrated (i.e. > 5 bits per single phase-change cell). The ability to support multiple levels significantly improves the storage density capabilities of any memory, and so an obvious question is whether or not the plasmonic photonic memory described here can also support multilevel states.

To address the issue of multilevel storage in the plasmonic cell we consider a 4-level (i.e. 2 bit per cell) system in which information is stored in the fractional crystallization of the cell. More specifically we assume memory levels 0, 1, 2 and 3 are stored by fractionally crystallized volumes (X), of 1.0, 0.72, 0.44 and 0.18 (i.e. the range of X from 0.18 to 1 is divided into four equally spaced levels). Next, we perform a type of *reset* operation, using a single 1 mW, 2 ns optical pulse. This has the effect of resetting the crystal fraction in the cell to the lowest value (i.e. $X = 0.18$), whichever of the other three states the cell was previously in (i.e. it is reset to $X = 0.18$ from $X = 0.44$, 0.72 or 1.0 using the same *reset* pulse), as shown in Fig. 8(a). After the application of such a *reset* pulse, we apply a double- step pulse of the type described in the previous section, i.e., a 1.5 ns pulse of 1.5 mW, followed immediately by a pulse with linearly decreasing power from 1.2 mW to 0.5 mW. By terminating the linearly decaying pulse at different times (here after 10.2, 12.4, 13.8 and 16.5 ns) we can store in the cell the chosen fractionally crystallized values of $X = 0.18$, 0.44, 0.72 or 1.0, as shown in Fig. 8(b). The resulting distribution of crystallized material within the GST cell for these 4-levels is depicted in Fig. 8(c) –8(g). Indeed, using the above approach we can control quite precisely the crystal fraction in phase-change cell and so could expect to store significantly more than the 4-levels examined here. However, we note that obtaining the necessary starting, or reset, condition of Fig. 8(a) using a single reset pulse (i.e., having an identical reset pulse whatever the previous state of the phase-change cell) becomes more difficult for a higher number of levels.

Finally, we note that the energies required to record the 4 levels above correspond to 10.8, 12.4, 13.4 and 15 pJ respectively, again significantly lower than in conventional device architectures (see Table 3). Moreover, the readout contrast is good, with a contrast separation between levels of approximatively 4.2% and an almost linear relationship between contrast and the fraction of crystallization in the cell (see inset in Fig. 8(b)), the latter indicating that significantly more than four levels could also be adequately distinguished from each other in the readout process.

Optics EXPRESS

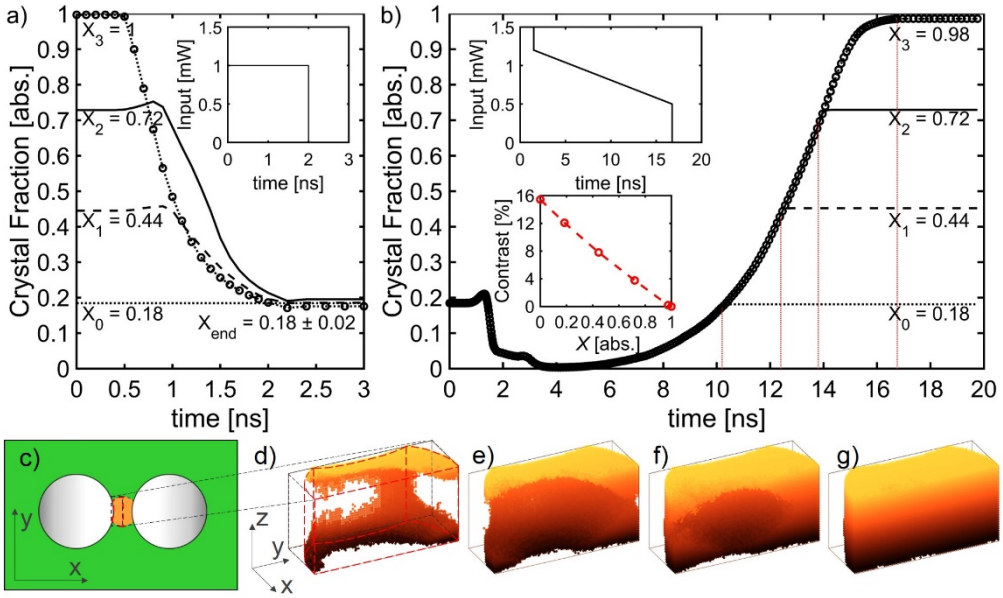

Fig. 8. 4-level storage demonstration, using the same plasmonically-enhanced cell configuration as in Fig. 6. (a) Variation of the crystal fraction X during the *reset* operation in which a 1 mW, 2 ns rectangular optical pulse initializes the cell crystal fraction to $X = 0.185 \pm 0.01$ when starting from any of the assumed X levels of 0.18, 0.44, 0.72 and 1. (b) Crystal fraction, X, during the application of a double step pulse (a pulse of 1.5 mW for 1.5 ns, followed by 15 ns of linearly decreasing power from 1.2 mW to 0.5 mW), showing that the desired four multilevel states of $X = 0.18$, 0.44, 0.72 and 1 are achieved by termination of the excitation pulse after 10.2 ns, 12.4 ns, 13.8 ns and 16.5 ns respectively. The inset reports the dependency of X and the (room-temperature) optical readout contrast. (c-g) The spatial distribution of crystallized material within the GST cell for (d) $X = 0.18$, (e) $X = 0.44$, (f) $X = 0.72$ and (g) $X = 0.98$ and resulting from the *erase* operation reported in Fig. 8(b). Note that only (left) half of the GST cell is shown here, as shown in (c), with the crystallization distribution being mirrored in the center-plane of the cell (note that all colors in (d) to (g) represent crystalline regions, the different colors used only to aid visualization of the time-evolution of the crystallized region).

5. Conclusions

In conclusion, we have shown that by using plasmonic enhancement we can greatly increase the strength of the light-matter interaction occurring in integrated phase-change photonic memory cells. Via simulation, we showed the existence of strong dipolar and quadrupolar plasmonic resonances for a structure consisting of a circular dimer nanoantenna deposited on top of a silicon nitride ridge waveguide, with electric field enhancement factors as high as 1000 and more. With the gap region between the nanoantenna discs filled with phase-change material, specifically $Ge_2Sb_2Te_5$, we could provide both binary and multilevel memory capabilities, with a much improved switching performance (increased switching speed and reduced switching energies) as compared to more conventional (non-plasmonic) device architectures. More specifically, write/erase speeds in the range 2 to 20 ns and write/erase energies in the range 2 to 17 pJ were predicted, representing improvements of one to two orders of magnitude when compared to conventional device architectures. This comes though at the cost of increased fabrication complexity.

Optics EXPRESS

Funding

Horizon 2020 Framework Programme (780848); Engineering and Physical Sciences Research Council (EP/L015331/1, EP/M015173/1, EP/M0151301/1); Deutsche Forschungsgemeinschaft (PE1832/5-1).

Data access

Data relating to this paper can be obtained via the University of Exeter's online repository at https://ore.exeter.ac.uk/repository, or from the corresponding author upon reasonable request.

References

1. C. Sun, M. T. Wade, Y. Lee, J. S. Orcutt, L. Alloatti, M. S. Georgas, A. S. Waterman, J. M. Shainline, R. R. Avizienis, S. Lin, B. R. Moss, R. Kumar, F. Pavanello, A. H. Atabaki, H. M. Cook, A. J. Ou, J. C. Leu, Y. H. Chen, K. Asanović, R. J. Ram, M. A. Popović, and V. M. Stojanović, "Single-chip microprocessor that communicates directly using light," Nature **528**(7583), 534–538 (2015).
2. A. Alduino and M. Paniccia, "Wiring electronics with light," Nat. Photonics **1**(3), 153–155 (2007).
3. R. Kirchain and L. Kimerling, "A roadmap for nanophotonics," Nat. Photonics **1**(6), 303–305 (2007).
4. K. Nozaki, A. Shinya, S. Matsuo, Y. Suzaki, T. Segawa, T. Sato, Y. Kawaguchi, R. Takahashi, and M. Notomi, "Ultralow-power all-optical RAM based on nanocavities," Nat. Photonics **6**(4), 248–252 (2012).
5. E. Kuramochi, K. Nozaki, A. Shinya, K. Takeda, T. Sato, S. Matsuo, H. Taniyama, H. Sumikura, and M. Notomi, "Large-scale integration of wavelength-addressable all-optical memories on a photonic crystal chip," Nat. Photonics **8**(6), 474–481 (2014).
6. T. Alexoudi, D. Fitsios, A. Bazin, P. Monnier, R. Raj, A. Miliou, G. T. Kanellos, N. Pleros, and F. Raineri, "III-V-on-Si Photonic Crystal Nanocavity Laser Technology for Optical Static Random Access Memories," IEEE J. Sel. Top. Quantum Electron. **22**(6), 295–304 (2016).
7. W. H. P. Pernice and H. Bhaskaran, "Photonic non-volatile memories using phase change materials," Appl. Phys. Lett. **101**(17), 171101 (2012).
8. C. Rios, P. Hosseini, C. D. Wright, H. Bhaskaran, and W. H. P. Pernice, "On-chip photonic memory elements employing phase-change materials," Adv. Mater. **26**(9), 1372–1377 (2014).
9. C. Ríos, M. Stegmaier, P. Hosseini, D. Wang, T. Scherer, C. D. Wright, H. Bhaskaran, and W. H. P. P. Pernice, "Integrated all-photonic non-volatile multi-level memory," Nat. Photonics **9**(11), 725–732 (2015).
10. X. Li, N. Youngblood, C. Ríos, Z. Cheng, C. D. Wright, W. H. Pernice, and H. Bhaskaran, "Fast and reliable storage using a 5 bit, nonvolatile photonic memory cell," Optica **6**(1), 1–6 (2019).
11. J. Zheng, A. Khanolkar, P. Xu, S. Colburn, S. Deshmukh, J. Myers, J. Frantz, E. Pop, J. Hendrickson, J. Doylend, N. Boechler, and A. Majumdar, "GST-on-silicon hybrid nanophotonic integrated circuits: a non-volatile quasi-continuously reprogrammable platform," Opt. Mater. Express **8**(6), 1551–1561 (2018).
12. J. Feldmann, M. Stegmaier, N. Gruhler, C. Ríos, H. Bhaskaran, C. D. Wright, and W. H. P. Pernice, "Calculating with light using a chip-scale all-optical abacus," Nat. Commun. **8**(1), 1256 (2017).
13. Z. Cheng, C. Ríos, W. H. P. Pernice, C. D. Wright, and H. Bhaskaran, "On-chip photonic synapse," Sci. Adv. **3**(9), e1700160 (2017).
14. C. Ríos, N. Youngblood, Z. Cheng, M. Le Gallo, W. H. P. Pernice, C. D. Wright, A. Sebastian, and H. Bhaskaran, "In-memory computing on a photonic platform," Sci. Adv. **5**(2), u5759 (2019).
15. J. Von Keitz, J. Feldmann, N. Gruhler, C. Ríos, C. D. Wright, H. Bhaskaran, and W. H. P. Pernice, "Reconfigurable Nanophotonic Cavities with Nonvolatile Response," ACS Photonics **5**(11), 4644–4649 (2018).
16. S. A. Maier, P. G. Kik, H. A. Atwater, S. Meltzer, E. Harel, B. E. Koel, and A. A. G. Requicha, "Local detection of electromagnetic energy transport below the diffraction limit in metal nanoparticle plasmon waveguides," Nat. Mater. **2**(4), 229–232 (2003).
17. C. Haffner, W. Heni, Y. Fedoryshyn, J. Niegemann, A. Melikyan, D. L. Elder, B. Baeuerle, Y. Salamin, A. Josten, U. Koch, C. Hoessbacher, F. Ducry, L. Juchli, A. Emboras, D. Hillerkuss, M. Kohl, L. R. Dalton, C. Hafner, and J. Leuthold, "All-plasmonic Mach-Zehnder modulator enabling optical high-speed communication at the microscale," Nat. Photonics **9**(8), 525–528 (2015).
18. J.-C. Weeber, J. Arocas, O. Heintz, L. Markey, S. Viarbitskaya, G. Colas-des-Francs, K. Hammani, A. Dereux, C. Hoessbacher, U. Koch, J. Leuthold, K. Rohracher, A. L. Giesecke, C. Porschatis, T. Wahlbrink, B. Chmielak, N. Pleros, and D. Tsiokos, "Characterization of CMOS metal based dielectric loaded surface plasmon waveguides at telecom wavelengths," Opt. Express **25**(1), 394–408 (2017).
19. Y. Fang and M. Sun, "Nanoplasmonic waveguides: Towards applications in integrated nanophotonic circuits," Light Sci. Appl. **4**(6), 1–11 (2015).
20. F. Peyskens, A. Dhakal, P. Van Dorpe, N. Le Thomas, and R. Baets, "Surface Enhanced Raman Spectroscopy Using a Single Mode Nanophotonic-Plasmonic Platform," ACS Photonics **3**(1), 102–108 (2016).
21. M. Février, P. Gogol, G. Barbillon, A. Aassime, R. Mégy, B. Bartenlian, J.-M. Lourtioz, and B. Dagens, "Integration of short gold nanoparticles chain on SOI waveguide toward compact integrated bio-sensors," Opt. Express **20**(16), 17402–17410 (2012).
22. D. A. Mohr, D. Yoo, C. Chen, M. Li, and S.-H. Oh, "Waveguide-integrated mid-infrared plasmonics with high-

Optics EXPRESS

efficiency coupling for ultracompact surface-enhanced infrared absorption spectroscopy," Opt. Express **26**(18), 23540–23549 (2018).
23. J. S. Fakonas, H. Lee, Y. A. Kelaita, and H. A. Atwater, "Two-plasmon quantum interference," Nat. Photonics **8**(4), 317–320 (2014).
24. R. W. Heeres, L. P. Kouwenhoven, and V. Zwiller, "Quantum interference in plasmonic circuits," Nat. Nanotechnol. **8**(10), 719–722 (2013).
25. N. Farmakidis, N. Youngblood, X. Li, J. Tan, J. L. Swett, Z. Cheng, D. C. Wright, W. H. Pernice, and H. Bhaskaran, "Plasmonic nanogap enhanced phase change devices with dual electrical-optical functionality," arXiv preprint arXiv:1811.07651 (2018).
26. M. Rudé, R. E. Simpson, R. Quidant, V. Pruneri, and J. Renger, "Active Control of Surface Plasmon Waveguides with a Phase Change Material," ACS Photonics **2**(6), 669–674 (2015).
27. G. A. E. Vandenbosch and Z. Ma, "Upper bounds for the solar energy harvesting efficiency of nano-antennas," Nano Energy **1**(3), 494–502 (2012).
28. L. Lu, W. Dong, J. K. Behera, L. Chew, and R. E. Simpson, "Inter-diffusion of plasmonic metals and phase change materials," J. Mater. Sci. **54**(4), 2814–2823 (2019).
29. B. Gholipour, J. Zhang, K. F. MacDonald, D. W. Hewak, and N. I. Zheludev, "An all-optical, non-volatile, bidirectional, phase-change meta-switch," Adv. Mater. **25**(22), 3050–3054 (2013).
30. W. Frei, "Using Perfectly Matched Layers and Scattering Boundary Conditions for Wave Electromagnetics Problems," https://uk.comsol.com/blogs/using-perfectly-matched-layers-and-scattering-boundary-conditions-for-wave-electromagnetics-problems/.
31. E. Yalon, S. Deshmukh, M. Muñoz Rojo, F. Lian, C. M. Neumann, F. Xiong, and E. Pop, "Spatially Resolved Thermometry of Resistive Memory Devices," Sci. Rep. **7**(1), 15360 (2017).
32. E. Bozorg-Grayeli, J. P. Reifenberg, M. A. Panzer, J. A. Rowlette, and K. E. Goodson, "Temperature-dependent thermal properties of phase-change memory electrode materials," IEEE Electron Device Lett. **32**(9), 1281–1283 (2011).
33. S. Bai, Z. Tang, Z. Huang, and J. Wang, "Transient Thermoreflectance Measurement of Thermal Conductivity of Nanoscale Silicon Nitride Thin Films," in Proceedings of ASME 2007 5th International Conference on Nanochannels, Microchannels, and Minichannels (2009), pp. 457–460.
34. J. Cho, K. K. Chu, P. C. Chao, C. McGray, M. Asheghi, and K. E. Goodson, "Thermal conduction normal to thin silicon nitride films on diamond and GaN,"in Proceedings of Fourteenth Intersociety Conference on Thermal and Thermomechanical Phenomena in Electronic Systems (ITherm). (IEEE, 2014), pp. 1186–1191.
35. J. A. Kalb, "Crystallization kinetics in antimony and tellurium alloys used for phase change recording," University of Aachen (2001).
36. M. Stegmaier, C. Ríos, H. Bhaskaran, and W. H. P. Pernice, "Thermo-optical Effect in Phase-Change Nanophotonics," ACS Photonics **3**(5), 828–835 (2016).
37. S. G.-C. Carrillo, G. R. Nash, H. Hayat, M. J. Cryan, M. Klemm, H. Bhaskaran, and C. D. Wright, "Design of practicable phase-change metadevices for near-infrared absorber and modulator applications," Opt. Express **24**(12), 13563–13573 (2016).
38. C. D. Wright, L. Wang, P. Shah, M. M. Aziz, E. Varesi, R. Bez, M. Moroni, and F. Cazzaniga, "The Design of Rewritable Ultrahigh Density Scanning-Probe Phase-Change Memories," IEEE Trans. NanoTechnol. **10**(4), 900–912 (2011).
39. V. Bragaglia, B. Jenichen, A. Giussani, K. Perumal, H. Riechert, and R. Calarco, "Structural change upon annealing of amorphous GeSbTe grown on Si(111)," J. Appl. Phys. **116**(5), 054913 (2014).
40. A. Arbabi and L. L. Goddard, "Measurements of the refractive indices and thermo-optic coefficients of Si_3N_4 and $SiO(_x)$ using microring resonances," Opt. Lett. **38**(19), 3878–3881 (2013).
41. V. Palankovski and R. Quay, *Analysis and Simulation of Heterostructure Devices*, Computational Microelectronics (Springer, Wien, 2004).
42. M. B. Takeyama, M. Sato, Y. Nakata, Y. Kobayashi, T. Nakamura, and A. Noya, "Characterization of silicon nitride thin films deposited by reactive sputtering and plasma- enhanced CVD at low temperatures," Jpn. J. Appl. Phys. **53**(5S2), 05GE01 (2014)
43. J. Kischkat, S. Peters, B. Gruska, M. Semtsiv, M. Chashnikova, M. Klinkmüller, O. Fedosenko, S. Machulik, A. Aleksandrova, G. Monastyrskyi, Y. Flores, and W. T. Masselink, "Mid-infrared optical properties of thin films of aluminum oxide, titanium dioxide, silicon dioxide, aluminum nitride, and silicon nitride," Appl. Opt. **51**(28), 6789–6798 (2012).
44. F. Udrea, J. W. Gardner, D. Setiadi, J. A. Covington, T. Dogaru, C. C. Lu, and W. I. Milne, "Design and simulations of SOI CMOS micro-hotplate gas sensors," Sens. Actuators B Chem. **78**(1–3), 180–190 (2001).
45. P. Dong, T.-C. Hu, T.-Y. Liow, Y.-K. Chen, C. Xie, X. Luo, G.-Q. Lo, R. Kopf, and A. Tate, "Novel integration technique for silicon/III-V hybrid laser," Opt. Express **22**(22), 26854–26861 (2014).
46. P. B. Johnson and R. W. Christy, "Optical Constants of the Noble Metals," Phys. Rev. B **6**(12), 4370–4379 (1972).
47. G. T. Furukawa, M. L. Reilly, and J. S. Gallagher, "Critical Analysis of Heat—Capacity Data and Evaluation of Thermodynamic Properties of Ruthenium, Rhodium, Palladium, Iridium, and Platinum from 0 to 300K. A Survey of the Literature Data on Osmium," J. Phys. Chem. Ref. Data **3**(1), 163–209 (1974).
48. Z. Cheng, L. Liu, S. Xu, M. Lu, and X. Wang, "Temperature dependence of electrical and thermal conduction in single silver nanowire," Sci. Rep. **5**(1), 10718 (2015).

Optics EXPRESS

49. S. Lovell and E. Rollinson, "Density of Thin Films of Vacuum Evaporated Metals," Nature **218**(5147), 1179–1180 (1968).
50. C. Rios, M. Stegmaier, Z. Cheng, N. Youngblood, C. D. Wright, W. H. P. Pernice, and H. Bhaskaran, "Controlled switching of phase-change materials by evanescent-field coupling in integrated photonics [Invited]," Opt. Mater. Express **8**(9), 2455–2470 (2018).
51. C. Wu, H. Yu, H. Li, X. Zhang, I. Takeuchi, and M. Li, "Low-Loss Integrated Photonic Switch Using Subwavelength Patterned Phase Change Material," ACS Photonics **6**(1), 87–92 (2019).
52. I. Hilmi, E. Thelander, P. Schumacher, J. W. Gerlach, and B. Rauschenbach, "Epitaxial Ge 2 Sb 2 Te 5 films on Si(111) prepared by pulsed laser deposition," Thin Solid Films **619**, 81–85 (2016).
53. C. Peng, L. Cheng, and M. Mansuripur, "Experimental and theoretical investigations of laser-induced crystallization and amorphization in phase-change optical recording media," J. Appl. Phys. **82**(9), 4183–4191 (1997).
54. J. Orava, A. L. Greer, B. Gholipour, D. W. Hewak, and C. E. Smith, "Characterization of supercooled liquid $Ge_2Sb_2Te_5$ and its crystallization by ultrafast-heating calorimetry," Nat. Mater. **11**(4), 279–283 (2012).
55. M. Stegmaier, C. Ríos, H. Bhaskaran, C. D. Wright, and W. H. P. Pernice, "Nonvolatile All-Optical 1 × 2 Switch for Chipscale Photonic Networks," Adv. Opt. Mater. **5**(1), 1600346 (2017).

109.54.42.232 {ts '2024-06-28 15:51:32'}